



# Stability and Stress-Deformation Analyses of Reinforced Slope Failure at Yeager Airport

James G. Collin, Ph.D., P.E., D.GE, F.ASCE<sup>1</sup>; Timothy D. Stark, Ph.D., P.E., D.GE, F.ASCE<sup>2</sup>;  
Augusto Lucarelli, M.ASCE<sup>3</sup>; Thomas P. Taylor, Ph.D., P.E., D.GE, F.ASCE<sup>4</sup>;  
and Ryan R. Berg, P.E., D.GE, F.ASCE<sup>5</sup>

**Abstract:** This paper describes the material properties along with the inverse limit-equilibrium and permanent deformation analyses used to investigate the 2015 reinforced slope failure at the Yeager Airport near Charleston, West Virginia. Inverse two-dimensional (2D) limit-equilibrium analyses were first performed to evaluate laboratory-derived strength parameters, slope geometry, and soil reinforcement configuration that would reproduce the observed critical failure surface. Because of the shape of the reinforced soil slope (RSS) (outside radius), the impact of the direction of the uniaxial geogrid reinforcement, varying from parallel to almost perpendicular to the direction of sliding, was analyzed using a three-dimensional (3D) limit-equilibrium analysis. Finite-difference permanent deformation analyses were also conducted to understand the internal stresses and deformations of the RSS prior to failure and kinematics of the slope failure. The results of these various analyses are consistent with postfailure field observations and demonstrate the value of performing multiple types of analyses, e.g., 2D and 3D limit-equilibrium and permanent deformation analyses, when analyzing a complex slope failure. DOI: [10.1061/\(ASCE\)GT.1943-5606.0002454](https://doi.org/10.1061/(ASCE)GT.1943-5606.0002454). © 2020 American Society of Civil Engineers.

**Author keywords:** Geogrids; Inverse analysis; Shear strength; Anisotropy; Slope stability; Compacted fill; Fully softened strength; Residual strength; Strength-reduction method; Numerical analysis.

## Introduction

Yeager Airport near Charleston, West Virginia, was constructed atop mountainous terrain in 1947. Construction of the airport involved excavating several hilltops and filling the adjacent valleys to create a nearly horizontal plateau for the runways, taxiways, roads, and accompanying infrastructure. The earthwork required 3 years to complete and at the time was the second largest earth-moving project in history, but well behind the Panama Canal (Lostumbo 2010). The earthwork involved moving more than 6.88 million m<sup>3</sup> (9 million cu yd) of earth and rock and required more than 910,000 kg (2 million lb) of explosives to facilitate rock excavation (Lostumbo 2010). Because the airport was constructed on hilltop ridges, the ground surface slopes steeply down to the surrounding Elk and Kanawha River Valleys.

To comply with new airport regulations, Yeager Airport was required to extend Runway 5 by 150 m (500 ft) to create a longer emergency stopping area. This was quite a challenge because the runway extension would be over a 91-m (300-ft)-high steep slope. A reinforced steepened slope was selected to extend the runway instead of other options because it offered an economical solution that was believed to be easy to construct and blend in with the surrounding green hills of West Virginia (Lostumbo 2010). This resulted in the tallest [72 m (240 ft)] 1H:1V (45°) geosynthetic reinforced vegetated slope known in the United States in 2007 when it was completed (Lostumbo 2010). Unfortunately, the slope failed in 2015, 8 years after construction.

The reinforced soil slope (RSS) was constructed with a primary and secondary zone of geogrid reinforcement. The primary reinforcement, strips of polyester uniaxial geogrids, was used to construct the majority of the RSS. Two types of uniaxial geogrids were used in the primary reinforcement zone, namely 10G and 20G geogrids with long-term allowable tensile strengths, i.e., ultimate strengths reduced for installation damage, of 49.6 kN/m (3,400 lb/ft) and 66.1 or 145.9 kN/m (4,530 lb/ft), respectively.

Fig. 1(a) shows a layer of the black primary geogrid being placed below the slope crest. Fig. 1(a) also shows the secondary reinforcement zone, which was used to support the face of the RSS and consisted of a lightweight geogrid face wrap. This lightweight geogrid consists of a small-aperture mesh-type geogrid comprised of a green woven polypropylene mesh that provided erosion protection and allowed for fast germination of the vegetation on the slope face (Lostumbo 2010).

The constructed reinforced slope started to show movement about 2 years prior to failure, with cracks first appearing in the crest of the slope along the back of the RSS mass in 2013, or 6 years after completion. By February 2014, large deformations and tension cracks were visible in the slope crest and runway. The slope failed on March 12, 2015 (Fig. 1), after 8 years of service. This paper

<sup>1</sup>President, Collin Group, 7445 Arlington Rd., Bethesda, MD 20184. Email: [jim@thecollingroup.com](mailto:jim@thecollingroup.com)

<sup>2</sup>Professor, Dept. of Civil and Environmental Engineering, Univ. of Illinois at Urbana-Champaign, 205 N. Mathews Ave., Urbana, IL 61801 (corresponding author). ORCID: <https://orcid.org/0000-0003-2384-1868>. Email: [tstark@illinois.edu](mailto:tstark@illinois.edu)

<sup>3</sup>Principal, Itasca Consulting Group, Inc., 111 3rd Ave. South, Suite 450, Minneapolis, MN 55401. Email: [alucarelli@itascacg.com](mailto:alucarelli@itascacg.com)

<sup>4</sup>Civil Engineering Consultant, Ground Improvement Systems, LLC 2301 Poplar LN Colleyville, TX 76034. ORCID: <https://orcid.org/0000-0001-7828-2894>. Email: [tpataylor.pe@gmail.com](mailto:tpataylor.pe@gmail.com)

<sup>5</sup>President, Ryan R Berg & Associates, 2190 Leyland Alcove, Woodbury, MN 55125-3504. ORCID: <https://orcid.org/0000-0002-7013-0711>. Email: [ryanberg@att.net](mailto:ryanberg@att.net)

Note. This manuscript was submitted on April 1, 2020; approved on September 15, 2020; published online on December 28, 2020. Discussion period open until May 28, 2021; separate discussions must be submitted for individual papers. This paper is part of the *Journal of Geotechnical and Geoenvironmental Engineering*, © ASCE, ISSN 1090-0241.

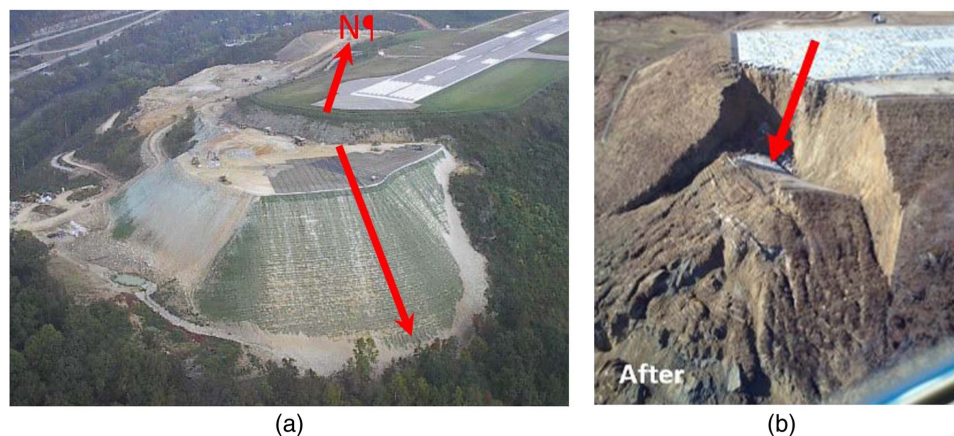


**Fig. 1.** Geogrid reinforced slope at Yeager Airport: (a) during construction with uniaxial geogrids being placed horizontally and overlapped at the top of the fill slope (Reprinted from *Lostumbo 2010*, © ASCE); and (b) after failure on March 12, 2015, with direction of slope movement indicated by an arrow (Image by James G. Collin).

presents the two-dimensional (2D) and three-dimensional (3D) inverse limit-equilibrium analyses of the slope failure to quantify the impact of various design assumptions and changes during construction on the stability of this RSS. Finite-difference permanent deformation analyses were also conducted to understand the internal stresses and deformations of the RSS prior to failure and kinematics of the slope failure [more details on the design, construction, post-construction exploration program, and causes of failure have been given by Berg et al. (2020)].

The 3D limit-equilibrium analyses accounted for the 3D driving forces, overlapping geogrids, anisotropic geogrid tensile resistance caused by selection of uniaxial geogrids, use of different types of uniaxial geogrids, 3D slope and groundwater conditions, and construction damage to the geogrids involved in this RSS. Values of 2D and 3D factors of safety (FS) were calculated for five slope conditions to quantify the decrease in FS from the initial design to the time of slope failure: (1) initial design, (2) revised design, (3) end of construction peak soil strength, (4) end of construction fully softened strength (FSS), and (5) failure. A FLAC3D version 7.00 slice

model was also developed to analyze the excavation and construction stages of the RSS, and then a strength-reduction analysis was performed along the soil-rock interface where the failure surface occurred to better understand the propagation of the failure.

### Slope Geometry, Geogrid Layout, and Material Properties

Fig. 2 shows a typical design cross section of the reinforced slope, depicting the existing slope face prior to construction of the RSS and the extent of the rock excavation necessary to accommodate the specified primary uniaxial geogrid reinforcement lengths. In the original design, the primary uniaxial geogrids extended 53.4 m (175 ft) from the slope face into the reinforced slope after excavating some of the existing bedrock. The location of the cross section shown in Fig. 2 is near the slope nose [arrow in Fig. 1(b)], which is in the direction of movement and the tallest portion of the RSS. The primary uniaxial geogrid 20G was used for the entire height of the

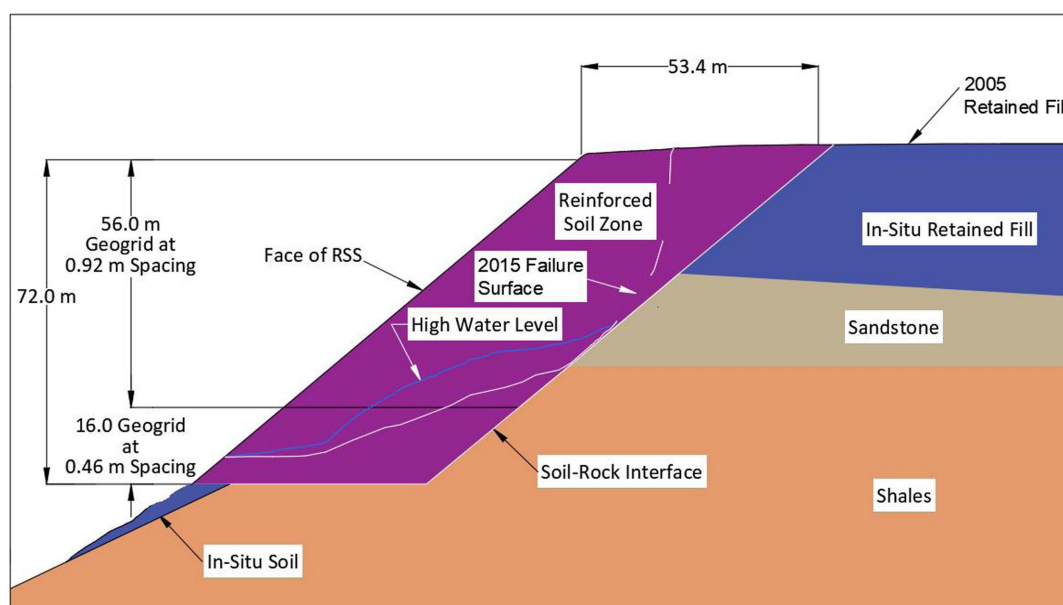


**Fig. 2.** Original design cross section.

**Table 1.** Engineering parameters used in stability analyses

Stability analysis case	Slope material	Moist unit weight, $\gamma_{\text{moist}}$ (kN/m <sup>3</sup> )	Effective stress friction angle, $\phi'$ (degree)	Effective stress cohesion, $c'$
S1: initial design	Reinforced soil zone	21.2	36	0
	In situ retained soil	21.2	36	0
S2: end of constructed (interface peak strength)	Reinforced soil zone	21.2	36	0
	In situ soil at slope toe	21.2	36	0
	Bearing soil at slope toe	21.2	36	0
	Soil–rock interface	21.2	36	0
S3: at failure (interface fully softened strength)	Reinforced soil zone	21.2	36	0
	In situ soil at slope toe	21.2	36	0
	Bearing soil at slope toe	21.2	36	0
	Soil–rock interface	21.2	Stress-dependent strength envelope	0

slope at this cross section. The geogrid was placed every 0.46 m (1.5 ft) in vertical height for the bottom 16 m of the RSS; the vertical spacing of the primary geogrid for the remainder of the RSS was placed every 0.91 m (3.0 ft) vertically. This resulted in 85 layers of 20G geogrid.

The native soils mainly consisted of residual sand and weathered bedrock. The reinforced fill was to be placed directly on the excavated sedimentary bedrock. The exposed bedrock consists mainly of native sandstones and shales, with some coal seams. For the inverse stability analysis, the competent rock material is considered to be of high strength so potential failure surfaces did not pass through but along the interface between the native rock and reinforced fill or through the geogrids and/or compacted soil at the rock interface.

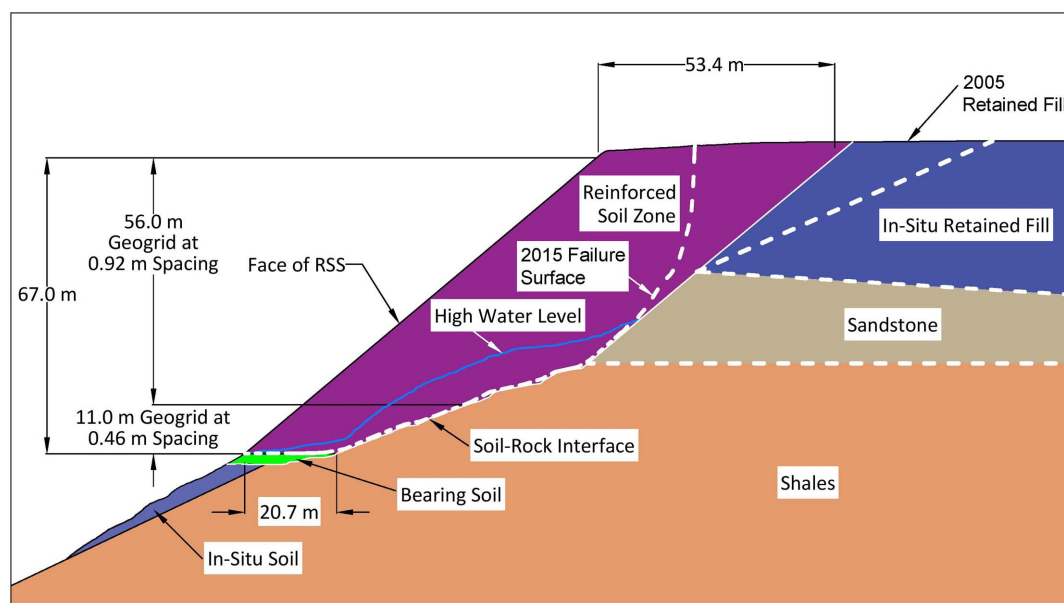
The initial design divided the slope into the following three material types for the slope stability analyses: (1) reinforced soil zone (Soil zone 1), (2) in situ retained fill (Soil zone 2), and (3) bearing soil at the slope toe (Soil zone 3) (Fig. 2; Table 1). The reinforced soil zone consists of compacted granular fill between layers of primary geogrid reinforcement, i.e., 10G and 20G uniaxial geogrids. No drainage was included in the design either below or behind the reinforced soil zone. The in situ retained soil zone is the soil behind the reinforced soil zone at the top of the slope (Fig. 2). The original design called for the base of the RSS to be founded

on rock. However, a field modification resulted in the bottom of the RSS being placed on approximately 3 m (10 ft) of unreinforced fill, i.e., the bearing soil zone at slope toe in Fig. 3.

During construction, another field change was made to the geogrid length to eliminate rock excavation anticipated in the original design. The lengths of the primary geogrids in the bottom of the RSS were shortened from 53.4 m (175 ft) to a minimum length of 20.7 m (68 ft) (Fig. 3).

An extensive postfailure forensic exploration was conducted to locate the failure surface and obtain samples of the primary geogrids, bearing soil at the slope toe, and soil–rock interface for laboratory testing. In particular, trench excavations were performed as part of the forensic investigation along the rock–soil failure surface (Fig. 3) at the base of the RSS. These trenches revealed that the soil–rock interface zone was comprised of degraded sedimentary shale, i.e., clay, below the RSS. The trench excavations also revealed that sliding occurred in the soil–rock interface zone behind the RSS in the lower portion of the slope. As a result, the stability of the slope was contingent upon the shear strength of the soil–rock interface, not the RSS.

To reflect the observed failure surfaces in the soil–rock interface, the critical failure surface shown in Fig. 3 passes along the bottom of the RSS along the soil–rock interface, then along the sandstone interface, and then up through the primary geogrid

**Fig. 3.** As-built cross section.



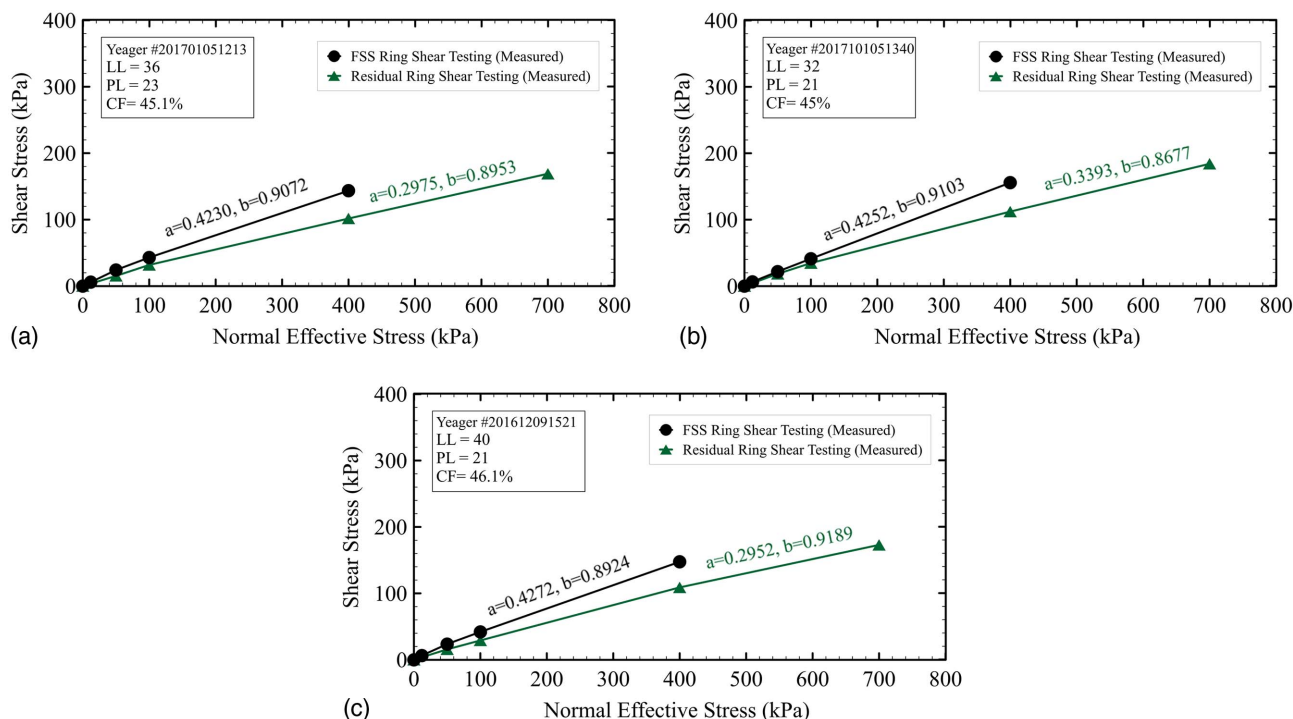


**Fig. 4.** Normal effective stress and FSS and residual strength envelopes for soil–rock interface zone for soil material Case S3 using samples obtained postfailure: (a) 201612091521; (b) 201701051213; and (c) 201701051340.

reinforcement, i.e., a rupture failure of the geogrids, until it daylighted at the top of the slope. As a result, samples of the soil–rock interface failure surface materials were obtained from the trench excavation for laboratory testing. These failure surface samples were tested to determine their fully softened and residual strengths for use in the stability and deformation analyses described subsequently.

Fig. 4 shows the measured drained FSS and residual envelopes measured for Trench samples 201612091521, 201701051213, and 201701051340 of the soil–rock interface. The resulting soil properties utilized in the stability and deformation analyses are presented in Table 1. For comparison purposes, the FSS and residual strength (RS) strength envelopes from empirical correlations are presented with the measured strengths for the three trench samples, and there is agreement between the strength envelopes. Fig. 4 also shows the power function coefficients  $a$  and  $b$  developed for the measured FSS and residual strength envelopes following the equation of Lade (2010), which is a transformation of the power function of Mesri and Shahien (2003) as follows:

$$\tau_{\text{FSS}} = a \times P_a \left( \frac{\sigma'_n}{P_a} \right)^b \quad (1)$$

where  $a$  = tangent of the secant friction angle at one atmosphere;  $\sigma'_n$  = any effective normal stress;  $P_a$  = atmospheric pressure in the same units as  $\sigma'_n$ , e.g., 101.3 kPa; and  $b$  = stress-dependency or curvature of the strength envelope and is equivalent to the  $m_{fs}$  parameter from Mesri and Shahien (2003) for a FSS strength envelope. The use of this power function allows the creation of a stress-dependent strength envelope at more effective normal stresses than 0, 12, 50, 100, 400, and 700 kPa used for the FSS and residual testing. The resulting  $a$  and  $b$  coefficients were used to generate the strength envelopes used in the stability and stress-deformation analyses described subsequently.

To model the five analysis cases representative of the history of the RSS, i.e., initial design through failure, the strength of

the primary geogrids was varied to match the condition being analyzed for each case. The long-term design strength values of the 10G and 20G geogrids used in the analysis for the as-designed case were based on published data from the geogrid manufacturer and are listed in Table 2. This is referred to as Analysis case G1 in Table 2.

Laboratory tensile testing on exhumed 10-year-old primary geogrid samples was conducted during this forensic study to determine the average machine direction (MD) tensile strength at the time of slope failure. As a consequence, these test results include the impact of construction damage. The measured MD tensile strengths for the exhumed 10G and 20G geogrids are 131.3 kN/m (9,000 lb/ft) and 145.9 kN/m (10,000 lb/ft), respectively. This is referred to as Analysis case G2 in Table 3 and reflects the tensile strengths of the primary geogrids after installation damage but before long-term degradation.

In the week prior to the failure, a head scarp developed with a vertical offset of approximately 1 m (3 ft). This occurred within the reinforced soil mass, resulting in the development of creep strains in the geogrid reinforcement. Therefore, the third analysis case involves using the tensile strengths of the geogrid to reflect the effects of creep and installation damage at the time of failure. The strength

**Table 2.** Measured and estimated geogrid material properties

Analysis case	Geogrid type	Tensile strength in MD (kN/m)
G1: initial design minimum	20G	66.1
long-term design strength (LTDS)	10G	52.6
G2: designed geogrids	20G	145.9
accounts for installation damage	10G	131.3
G3: designed geogrids accounts	20G	84.8
for installation damage and creep	10G	78.6

**Table 3.** Five scenarios analyzed in 2D and 3D limit-equilibrium analyses

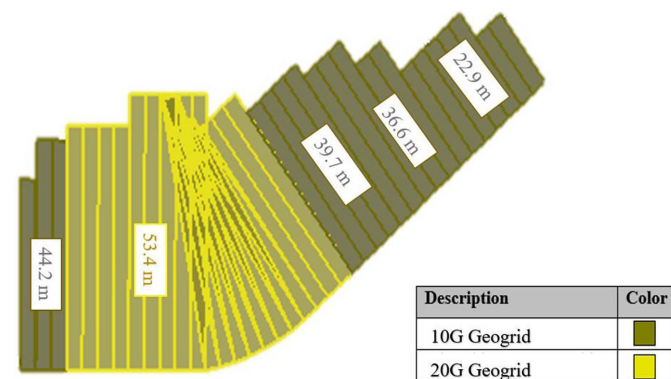
Case	Name	Scenario	Notes
1	Initial design	L1 + G1 + S1 + drained	Geogrid LTDS—uniform length
2	Revised design	L2 + G1 + S1 + drained	Geogrid LTDS—variable geogrid length
3	End of construction	L2 + G2 + S1 + drained	Exhumed geogrid—variable length
4	End of construction	L2 + G2 + S3 + GW	Exhumed geogrid—variable length
5	Failure	L2 + G3 + S3 + GW	Manufacturer geogrid values—variable length

Note: LTDS = long-term design strength.

of the exhumed geogrids as determined from the geogrid tensile tests was adjusted using reduction factors of 1.67 and 1.72 obtained from published information from the geogrid manufacturer for the 10G and 20G geogrids, respectively, to account for creep strains in the geogrid strips. This is referred to as Analysis case G3 in Table 3, and the tensile strengths of 78.6 kN/m (5,389 lb/ft) and 84.8 kN/m (5,814 lb/ft) reflect the tensile strengths of the geogrids prior to failure when creep and construction damage is considered.

Additional geogrid testing was performed during this forensic study to quantify the anisotropic tensile properties of the 10G and 20G geogrids. These tests show that the tensile strengths in Table 2 decreased linearly from the maximum to the minimum tensile resistance in the cross-machine direction (XMD). In the XMD, the geogrids exhibit a tensile strength that is only 10% of the tensile strength in the MD. This 90% reduction was reached when the angle of loading between the MD and XMD was approximately 60° from the MD. As a result, in the 3D stability analyses, the tensile strength of the geogrid was reduced 90% when the direction of slope movement and the as-constructed geogrid orientation was 60° or greater. After decreasing 90%, the tensile resistance was maintained at this minimum value until the direction of slope movement was parallel to the XMD. The geogrid layout pattern obtained from construction sketches (Fig. 5) was used to compute the angle between the MD of each geogrid strip and the direction of slope movement [arrow in Fig. 1(b)] to apply the anisotropic strength in the 3D stability analysis.

The 2D limit-equilibrium (LE) analyses were performed at the cross-section location shown in Fig. 1 and using the as-built cross section in Fig. 3. At the location of this cross section, the 20G geogrid was used for the full height of the RSS. The 10G geogrid was used in the upper portions of the RSS near the eastern and western edges of the slope where the slope height decreases. The overlap of the geogrids is concentrated at the slope nose where the slope curvature is the greatest, and only the 20G geogrids were used, and the geogrids extended far enough back into the fill to overlap each other.

**Fig. 5.** Geogrid layout diagram created during construction at elevation 281.5 m (+923 ft) with different geogrid types (10G and 20G).

To account for the overlapping geogrids, anisotropic geogrid tensile resistance, and different types of uniaxial geogrids, the actual layout of the geogrid strips at each reinforcement elevation was input into a 3D LE model. Fig. 5 shows the layout of the geogrid strips at elevation +266.9 m (875 ft) in the RSS. The geogrids were unrolled from the slope face back toward the existing rock or soil backcut. Fig. 5 shows that the geogrids overlap each other in the curved portion of the slope and along the right or east side of the slope. Fig. 1(a) also presents the slope during construction, showing some of the geogrids overlapping near the top of the slope.

The geometrical properties of the geogrids, such as the geogrid strip dimensions (length and width) and layout, were derived from the construction sketches created by the design consultant (Fig. 5). The construction sketches provide the geogrid layouts for each elevation where geogrids were installed. Each sketch assigns a number to each geogrid strip used, length of each geogrid, type of each geogrid, and the approximate layout and overlap, if any, of the geogrids. Using these construction sketches and slope geometry from topographic surveys, a MATLAB version 9.7 script was written to compute the necessary coordinates of the individual geogrid strips for inclusion in the 3D slope stability model. These coordinates were inputted into SLIDE3 version 2019 to build a 3D model of the reinforced soil zone. Additionally, construction sketches show that all of the geogrid strips were placed adjacent to each other with no gaps between each strip, i.e., the geogrid coverage is 100%, which is also modeled in SLIDE3.

Groundwater measurements were not available prior to the slope failure; therefore estimates for a range of groundwater potentiometric surface were made for the about 8 years of service of the RSS. To model field conditions during the service life, three piezometric groundwater levels were considered as part of this forensic evaluation. Fig. 3 shows the high groundwater surface used in the 3D LE analyses.

The 2D and 3D LE analyses performed as part of this forensic investigation considered the five scenarios in Table 3. Each of these design and in-service scenarios are based on the structure geometry (L1 or L2), geogrid properties (G1, G2, or G3), soil-rock interface properties (S1, S2, or S3), and three groundwater conditions. L1 structure geometry is the as-designed case and corresponds to the original design that was shown in the contract plans and consists of geogrids with a uniform length of 53.4 m (175 ft) from the base of the RSS to the top of the RSS (Fig. 2). L2 structure geometry is the as-built case and corresponds to the change during construction that reduced the geogrid length from 53.4 m (175 ft) to 24.4 m (80 ft) in the lower portion of the slope (Fig. 3).

## Two- and Three-Dimensional LE Slope Stability Analyses

The 2D LE analyses were performed using the software programs SLIDE2 version 2019 (Rocscience (2018)) and SLIDE3.

The 2D LE methods do not incorporate shear resistance generated along the sides of the slide mass. Consequently, the computed

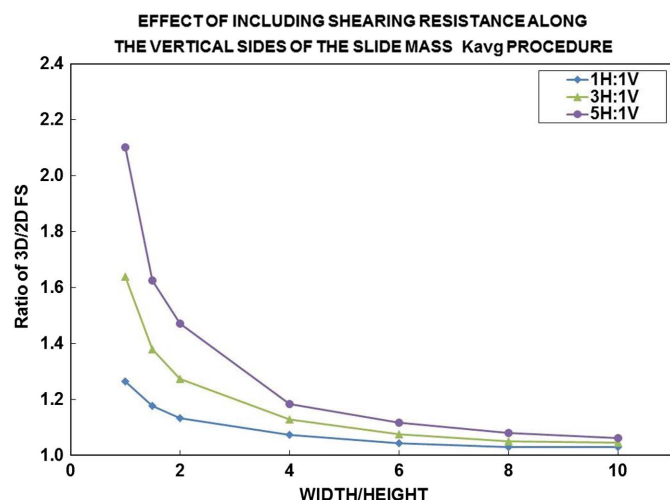


**Fig. 6.** Ratio of 3D to 2D factors of safety as a function of the width and height of the slope for translational failure surfaces (Adapted from Akhtar and Stark 2017).

2D FS underestimates the field FS especially for slopes with a width to height ratio of less than 6 (Arellano and Stark 2000). Study of several field case histories show that the difference between 2D and 3D FS is most pronounced in cases that involve a noncircular failure surface (Stark and Eid 1998) as in this case history. Akhtar and Stark (2017) show that the ratio of 3D to 2D FS ranges from 1.1 to 1.6 for a 3H:1V slope with width to height ratios of 2–6 (Fig. 6). This difference in 2D and 3D FS is useful for unreinforced slopes because it only accounts for differences in geometry, side forces, and material properties between the 2D and 3D analyses. The difference between 2D and 3D FS can be even greater in geogrid reinforced slopes because the geosynthetics usually exhibit anisotropic engineering properties and 2D analyses usually only consider the strongest or MD of the reinforcement.

The Cheng and Yip (2007) 3D slope stability method that extends the Janbu (1954) 2D slope stability method to 3D is incorporated into SLIDE3 to calculate the 3D FS. The Janbu (1954) stability method satisfies all three conditions of force equilibrium. SLIDE3 discretizes the slide masses into a series of vertical square-shaped columns in which the normal and shear stresses on the column bases are calculated from the vertical forces. SLIDE3 does not assume a predefined sliding direction as suggested by Huang et al. (2002) and Cheng and Yip (2007), but one can be assigned. For the 3D analysis conducted, a predefined failure surface that matches field observations of the failure surface was specified in SLIDE3. This failure surface was based on photographic evidence and post-failure observations during the subsurface exploration and trenching. SLIDE3 was allowed to vary the failure surface geometry between points of known location to create the critical 3D failure surface.

Whereas a horizontal interslice resultant force angle is assumed for the Bishop and Janbu stability methods, SLIDE3 uses a half-sine function for determining the intercolumn resultant force angle for the generalized limit-equilibrium (GLE) method and a constant angle for the analysis using Spencer's stability method (Spencer 1967) as coded by Rocscience (2017). In this study, the critical failure surface yielded from the search approach using a field derived failure surface was analyzed using the Spencer (1967) stability method to determine the most probable failure surfaces for the landslide sequence FS. The Spencer (1967) stability method satisfies all

the conditions of force and moment equilibrium and is suitable for noncircular failure surfaces, including the ellipsoidal surfaces used in this study.

In typical situations, a static 2D FS of 1.3 is used for temporary or low-risk slopes and 1.5 for permanent slopes, where subsurface conditions have been well established. However, these FS are not appropriate for use with 3D analyses because 3D analyses account for additional shear resistance that is generated along the sides of the slide mass. The contribution of the additional shear resistance can be significant in shallow slide masses or for translational slide masses with a width to height ratio less than 6, resulting in calculated values of 3D FS that are greater than the calculated 2D FS. To achieve the same level of safety or risk as a static 2D FS of 1.3 or 1.5, the user must use a greater minimum FS for 3D analyses.

Stark and Ruffing (2018) present three methodologies for selecting a comparable 3D FS for design purposes. The most conservative approach negates the additional sophistication of a 3D analysis method and may be appropriate for use in high-risk situations or projects where soil parameters are not well understood. The minimum 3D FS is given by the following equation:

$$FS_{3D,Min} = FS_{2D,Min} * \frac{3DFS}{2DFS}$$

An example of the minimum 3D FS to achieve a 2D FS of 1.5 is about 1.9 using the following expression for a 3H:1V slope with a width to height ratio of 2 and the chart shown in Fig. 6:

$$FS_{3D,Min} = FS_{2D,Min} * \frac{3DFS}{2DFS} = 1.5 * 1.25 = 1.9 \quad (2)$$

Postfailure observations show that the overall direction of slope movement occurred roughly perpendicular to the curved face of the reinforced slope [Fig. 1(a)]. The 3D resultant force from the stability analysis should be parallel to the main direction of the slope movement (Stark and Eid 1998). The arrow in Fig. 1(b) indicates the direction of movement of the slide mass. Fig. 1(a) also shows the due north arrow. Similar to Landfill unit B-19 at Kettleman Hills (Seed et al. 1990, 1993; Stark and Eid 1998), the 3D driving forces and shear resistance exerted by the surrounding soil mass are underpredicted by a 2D analysis, which also contributed to the initiative for performing this 3D slope stability analysis.

### Modeling Geosynthetic Reinforcement

There are two common methods for modeling the geosynthetic reinforcement in limit-equilibrium analyses, i.e., Methods A and B. Method A involves representing the geosynthetic reinforcement by a single force at the base of each vertical column in a 3D analysis or a vertical slice in a 2D analysis. In this method, the reinforcement forces are applied parallel to the initial direction of the reinforcement, which is horizontal for this RSS. Method B also represents the geosynthetic reinforcement by a single force at the base of each vertical column or slice but tangent to the initial direction of the reinforcement, i.e., parallel to the column or slice base. A third option is applying a single force that bisects the forces generated by Methods A and B. In this analysis, Method A was utilized, but the impact of using Method B was investigated by repeating the 3D analyses with Method B, and the resulting values of 3D FS did not vary significantly.

### Two-Dimensional LE Results

Table 4 presents the results of the 2D and 3D LE analyses. From the results of the 2D analyses, the following observations can be made:



- The initial and revised design cases both had 2D factors of safety around 1.5 (1.54 and 1.45) when the RSS was founded on rock (Design cases 1 and 2). Reducing the reinforcement lengths from the original 53.4 m (175 ft) to the as-built length of 24.4 m (80 ft) reduced the factor of safety of the slope by 0.11 or 7%.
- The 2D FS at the end of construction (Case 3) was higher than the initial and revised design (Design cases 1 and 2) because the strength of the geogrid in Case 3 considers only installation damage and not long-term degradation of the geogrid.
- Failure to construct the RSS on sound rock as designed (Design case 4) instead of bearing soil (Fig. 3), reduced the 2D FS to a critically low value, i.e., 1.13–1.15. For Case 4, the level of groundwater did not have a significant impact on the 2D FS.
- When the 1-m (3-ft) vertical offset of the head scarp developed, the ultimate strength of the geogrid was reduced to account creep strains, which reduced the 2D FS to about unity (0.95–1.03), indicating failure. This is in excellent agreement with the RSS failing shortly after the head scarp developed at the top of slope.

### Three-Dimensional LE Results

Comparing the values of isotropic 3D FS with the 2D isotropic results shows that the 3D FSs are greater than the 2D FS. The range in factor of safety between the 2D and 3D is between 4% and 20%. For Case 5, i.e., failure condition, the difference between the 2D and 3D is between 4% and 13%. Typically, a 3D FS will be about 10%–30% greater than the 2D FS depending on the slope width to height ratio for an unreinforced slope and geometry that does not have significant 3D effects on stability. This results in a conservative slope design because the 3D effects are not being considered and provide additional stability. The analyses presented herein show that the difference in 2D and anisotropic 3D FS is 0%–4%, which is due to the anisotropic behavior of the uniaxial geogrids being modeled and does not yield a conservative slope design as occurs with unreinforced slopes. This indicates that 3D slope and geogrid effects are an important design consideration and 3D stability analyses should be considered when designing tall reinforced slopes that have geometries that result in the primary direction of the reinforcement strength not being parallel to the direction of movement.

Additionally, the design factor of safety for a 3D analysis to be comparable to a 2D factor of safety of 1.5 would be 1.9 for the initial design case, but the 3D isotropic factor of safety is only 1.65. The 2D initial design case failure plane passed through all 85

of the geogrid layers. Therefore, if an isotropic 3D analysis was performed, it would have yielded too low of a FS to meet a 2D FS of 1.5 or even 1.3.

Each 3D slope scenario was analyzed with the tensile resistance of the geogrids modeled as isotropic and anisotropic to assess the difference in tensile resistance between the MD and XMD. Table 4 indicates that the 3D FS for the initial design are 1.65 and 1.52 using isotropic and anisotropic geogrid tensile resistances, respectively. In this scenario, accounting for the anisotropic tensile behavior of the geogrids results in a decrease in the 3D FS of 0.13 or about 8%. The results for all cases analyzed also reflect this decrease in the 3D FS in the range of 5%–13%. As a result, if anisotropic geogrids are being proposed, 3D stability should be considered to model the mobilized tensile resistance across the slope.

The contribution of the geogrid strength to stability is overstated with an assumption that the geogrid strength was isotropic. In other words, assuming the geogrid strength is isotropic results in an inflated factor of safety because the decrease in strength at orientations other than the MD is not considered. For example, a failure plane that crossed a strip of geogrid at a 45° angle (relative to its roll edge) would apply the tensile strength per unit width along this failure plane. This results in a roll width strength that is about three times greater than the anisotropic tensile strength. Thus, an assumption of isotropic geogrid strength will result in safety factors values being overstated.

Finally, Table 4 demonstrates that the 3D FS at the time of failure for the four groundwater scenarios considered ranges from 1.15 to 1.02 for the isotropic geogrid tensile-resistance cases. When anisotropic geogrid tensile strength is considered, the 3D FS ranges from 1.08 to 0.95. Fig. 7 shows the 3D FS and slide mass for the time of failure with the high groundwater scenario and anisotropic geogrid tensile strengths. Accounting for a rise in groundwater, anisotropic tensile resistance, and creep strains in the geogrid strips caused the 3D FS to decrease to near unity (1.0) for the dry, low, and medium groundwater (GW) conditions and below unity (1.0) for the high GW scenario (0.95) (Fig. 7). All of the values of 3D FS are well below the design 2D FS of 1.3 used by the RSS designer. The 3D stability analyses presented herein are in excellent agreement with field observations and conditions at the time of the reinforced slope failure.

In summary, the following two main observations can be made from the 3D inverse stability analyses described previously:

- Not accounting for the anisotropic tensile resistance of the geogrids in the five analysis cases resulted in a decrease in 3D FS from about 4% to 13% (Table 4) with an average of about 8%.

**Table 4.** Two- and three-dimensional factors of safety for Analysis cases 1–5

Design and analysis case	Groundwater condition	Geogrid tensile strength model	2D FS with isotropic tensile strengths <sup>a</sup>	3D FS with isotropic/anisotropic tensile strengths
1: initial design case	Dry	I/A	1.54	1.65/1.52
2: revised design case	Dry	I/A	1.45	1.51/1.44
3: end of construction case (peak)	Dry	I/A	1.70	1.95/1.75
4: end of construction case (fully softened strength)	Dry	I/A	1.15	1.43/1.27
	Low	I/A	1.15	1.42/1.26
	Medium	I/A	1.13	1.37/1.21
	High	I/A	1.13	1.27/1.13
5: head scarp development and failure	Dry	I/A	1.03	1.15/1.08
	Low	I/A	1.01	1.14/1.07
	Medium	I/A	0.99	1.09/1.03
	High	I/A	0.95	1.02/0.95

Note: I = isotropic; and A = anisotropic.

<sup>a</sup>All 2D analyses used isotropic geogrid strength.

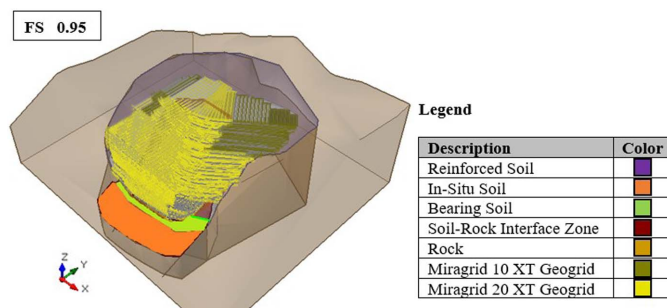


**Fig. 7.** SLIDE3 output for slope at time of failure with the high groundwater condition and anisotropic geogrid tensile strength.

- Failure of the slope was caused by a combination of the effects of anisotropic geogrid tensile resistance, shortened length of the geogrids to 24.4 m (80 ft) in the lower portion of the slope, reduction of the shear strength of the soil–rock interface zone from the peak to fully softened strength, reduction in the geogrid tensile strength due to construction damage and creep strains, and increased groundwater level from dry to medium conditions.

Accounting for the factors just listed, the 3D FS decreased from 1.95 at the end of construction with isotropic geogrid tensile resistance to unity (1.02), i.e., failure, with a high groundwater level and unity (1.03), i.e., failure, with anisotropic geogrid tensile resistance and a medium groundwater level.

The direction of the 3D resultant force for the critical 3D failure surface is 163°, which is measured from north in the clockwise direction [Fig. 1(b)]. The inclinations of the 3D resultant force for all the analyses are below 2° from the orientation of the critical 2D cross section. Comparing these inclinations with the critical 3D resultant force shows that the inclination of the 3D resultant force is in agreement with the direction of sliding, which validates the 3D FS (Stark and Eid 1998).

## Continuum Deformation Analyses

Fast Lagrangian Analysis of Continua (FLAC3D) is a 3D explicit finite-difference numerical program for engineering mechanics computations distributed by Itasca Consulting Group (2018). FLAC was originally developed for geotechnical and mining engineers, and its use has expanded into a variety of civil, mining, and mechanical engineering fields. The problem domain for the RSS structure is discretized in zones of different shapes and sizes. Each zone in the model behaves according to prescribed linear or nonlinear stress/strain properties in response to applied forces and boundary constraints. The RSS materials can yield and deform, and the numerical grid can deform and move with the material that it represents to differentiate the geogrids from the soils involved.

Limit-equilibrium analysis were performed to evaluate the factor of safety of the slope under various loading and material property conditions. The limit-equilibrium analyses described could not evaluate the stresses and deformations in the RSS prior to failure, which are helpful for understanding the kinematics of the failure. Because of the complex nature of the slope and geogrid reinforcement, FLAC3D was selected for the forensic analysis to further understanding of the failure kinematics.

The FLAC3D slice model (thickness of the model is 0.25 m) was built considering the results of the forensic subsurface exploration that identified the failure surface in the degraded soil–rock interface, i.e., clay, below the RSS (Fig. 3). The FLAC3D analysis

was performed for the Analysis case 4, i.e., end of construction in Table 4, and then a strength reduction of the soil–rock interface along the length of the shale rock strata was applied to the material until failure occurred to determine the mobilized strength of the soil–rock interface.

The ultimate strength [199.9 kN/m (13,705 lb/ft) for 20G] of the geogrid was used to model the construction stages of the RSS (Stage 2). Once the activation of the RSS layer was complete, the geogrid strength was reduced based on the exhumed geogrid test results [20G geogrid is 145.9 kN/m (10,000 lb/ft)]. This value was used in the FLAC3D analysis from Stage 3 onward. Geogrids are modeled with nonlinear cable elements that can yield and rupture if the strain limit is reached. During the strength-reduction analysis, if a cable element reached the limit tensile strain, it ruptured, and its contribution to the model was removed.

The power function coefficients  $a$  and  $b$  described previously were used to model the stress-dependent peak and FSS strength envelopes for the soil–rock interface failure surface materials in the permanent deformation analyses. This is accomplished by using a strength-reduction factor (SRF) in FLAC3D to model the stress-dependent strength envelopes for the soil–rock interface. A regression analysis gives an exponent  $b$  equal to 0.90, and the parameter  $a$  varied between 0.40 and 0.44. Fig. 8 shows how the strength envelope changes as a function of the  $a$  parameter. Reducing the  $a$  parameter allows modeling of the mechanical strength degradation of the lower soil–rock interface (Fig. 8). The reduction of the  $a$  parameter simulates the transition from a hypothetical peak soil–rock interface strength to a FSS.

The hypothetical peak strength used in this analysis provides a stable configuration for every groundwater condition, i.e., low, medium, and high phreatic were considered. The  $a$  parameter is reduced by applying a SRF to the initial value of  $a$  to simulate the reduction in soil–rock interface strength from peak to FSS and eventually to residual. The elastic modulus utilized in the analysis for the reinforced and retained backfill soils is 60,000 kPa. This modulus value was based on a sensitivity analysis in which the modulus was varied between 40,000 and 80,000 kPa to select a field representative value of 60,000 kPa. The elastic modulus for the bedrock was estimated using the following equation S:

$$E = (1.5 * e^5 + 2.0 * e^{4*z})^{0.8} \quad (3)$$

where  $z$  = depth from the original ground level before construction of the RS.

The FLAC3D model used the following construction sequence:

- Stage 1: stress initialization before RSS construction.
- Stage 2: excavation and construction of the RSS.
- Stage 3: application of the exhumed properties to the cable elements to represent the geogrid and four different groundwater conditions above the bedrock:
  1. Stage 3a: dry;
  2. Stage 3b: low;
  3. Stage 3c: intermediate; and
  4. Stage 3d: maximum.
- Stage 4: strength-reduction analyses of the lower soil–rock interface for the four groundwater cases:
  1. Stage 4a: dry;
  2. Stage 4b: low;
  3. Stage 4c: intermediate; and
  4. Stage 4d: maximum.

## FLAC3D Results

In Stage 3d, prior to initiating the SRF procedure, a significant volume of the RSS is already over 2% of the shear strain, potentially



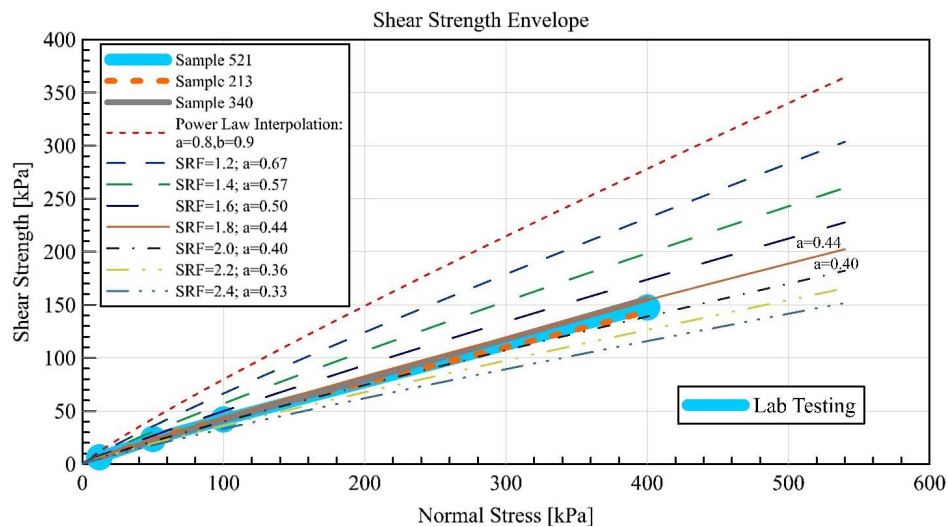


**Fig. 8.** Strength envelopes from laboratory testing and estimated using various values of power function coefficients  $a$  and  $b$ .

leading to crack formation at the ground surface (Fig. 7). There is a zone of large strain ( $>2\%$ ) that occurs in the model at the location where the initial tension cracks were observed, approximate 2 years before the failure, in the asphalt pavement above the RSS.

For illustration purposes, Fig. 9 shows the failure mechanism and the convergence ratio history during the strength-reduction process for Stage 4a. The model converges up to a SRF of 1.610 and becomes unstable after that point. The corresponding  $a$  parameter of the strength envelope is 0.497. The  $a$  parameter for the fully softened strength of the exhumed samples at the failure surface is between 0.4 and 0.44. This suggests that the slope failed with a mobilized shear of the soil–rock interface at or slightly above the FSS. Because there was no prior sliding, the mobilized interface strength is well above the residual strength as expected. Mobilizing an interface strength at or near the FSS is in agreement with the behavior of compacted fill slopes that fail shortly after or many years, e.g., 8 years in this case, later depending on the applied shear stresses and availability of water to cause the softening (Stark and Eid 1997).

Fig. 10 presents the failure mechanism for the Stage 4a analysis to investigate the deformation of the geogrids and slope during the slope failure. Fig. 10 shows that the geogrids failed in the head scarp area and two other downslope areas. These results also show movement occurring behind and below the geogrids in the lower portion of the slope, where field changes were made to the original design to shorten the geogrid in the bottom portion of the slope. All of these observations are in good agreement with field observations.

### Failure Mechanism

Based on the preceding discussion, the RSS collapsed in a compound (Berg et al. 1989) failure mode as the failure surface passed beneath the bottom layer of geogrid, partially behind (between about elevations of 216.6 and 252.6 m), and partially through, i.e., rupture of the geogrids, the reinforced soil mass (between about elevations 252.6 and 284.3 m). The failure surface beneath the RSS was along a shale–claystone interface. The RSS collapse

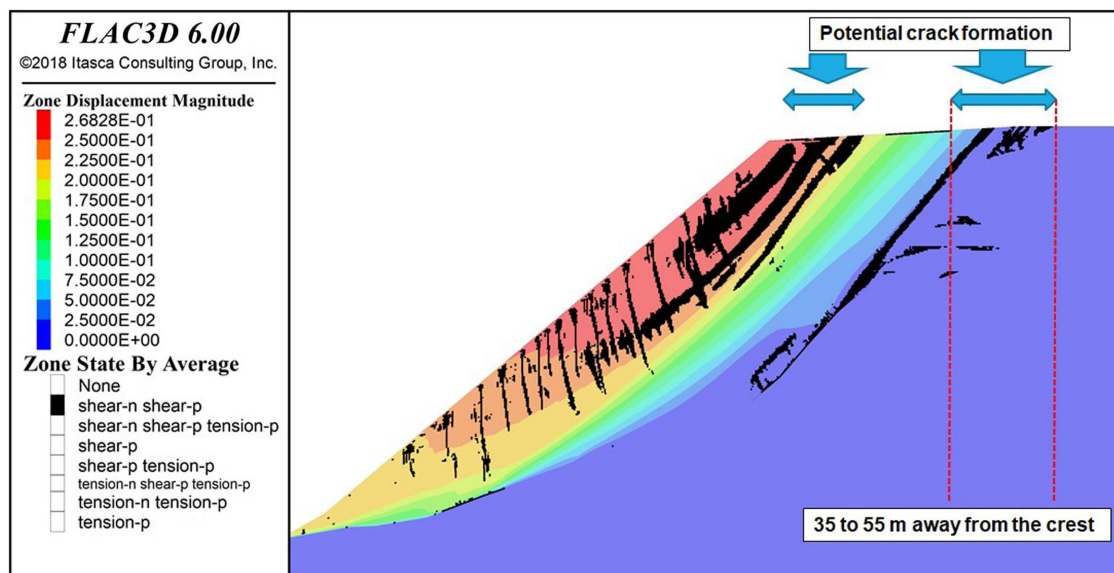


**Fig. 9.** Shear band development inside RSS at failure using FLAC3D.

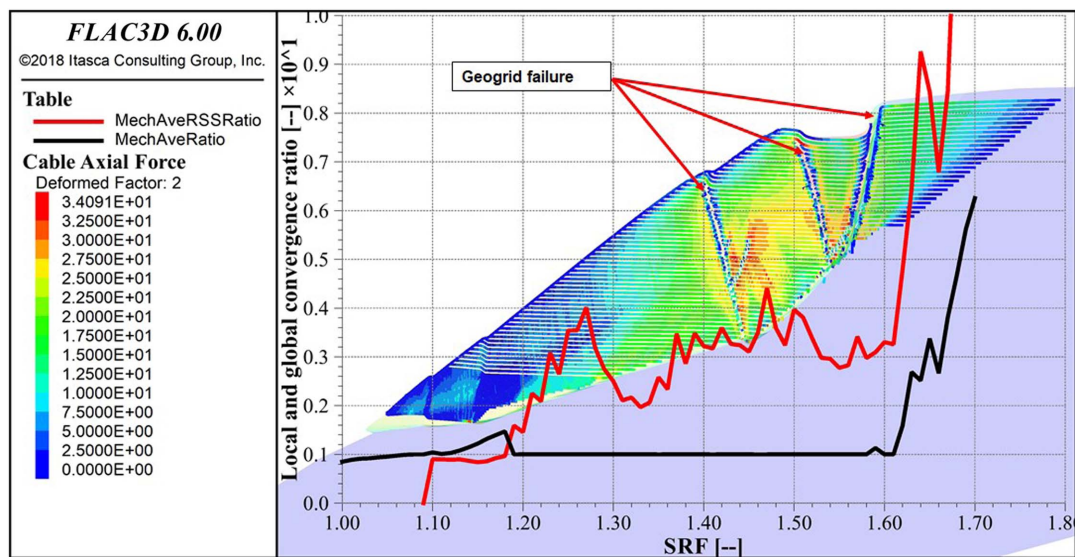


Fig. 10. Stage 4a failure mechanism using FLAC3D.

occurred after 8 years of in-service as the shear strength along the shale–claystone interface decreased from the peak value and to at or just above the fully softened strength.

The failure of this RSS is a result of many contributing factors and deficiencies (Collin et al., Yeager airport reinforced soil slope failure analysis, unpublished report; Berg et al. 2020). The primary contributing factors are (1) an insufficient surface exploration program and interpretation of data for design and detailing of the RSS; (2) the 3D aspects of the uniaxial geogrids were not addressed in the design; (3) insufficient foundation preparation and rock excavation and benching due to inadequate specifications and construction plan details; (4) founding the RSS on compacted soil instead of freshly excavated bedrock; (5) significantly shortening of the geogrid reinforcement length in the lower portion of the slope from 53.4 to 24.4 m; (6) deterioration of the soil–rock interface shear strength from the peak to FSS strength due to the high applied shear stresses and the presence of groundwater at the interface; and (7) inappropriate selection, testing, design, and analysis of uniaxial geogrids for this 3D structure.

The weak shale–claystone interface layers below the base of the RSS, which underwent strength reduction over time, were not identified in subsurface investigations, nor were they considered in design or removed during construction. The weak rock–soil interface layers and the failure to bench the rockface backcut significantly reduced the factor of safety of the RSS to a critical level and resulted in a compound failure mode collapse.

## Summary and Recommendations

This paper describes the material properties and inverse limit-equilibrium and stress-deformation analyses used to investigate the 2015 reinforced slope failure at the Yeager Airport near Charleston, West Virginia. The following are the main points derived from the 2D and 3D limit-equilibrium stability analyses and 3D deformation analysis:

- The results of the 2D and 3D limit-equilibrium analyses and 3D permanent deformation analyses are consistent with the failure mechanism identified in the postevent forensic subsurface investigation.

- The 3D LE analyses demonstrate that the anisotropic properties of uniaxial geogrid reinforcement when modeled as isotropic materials overpredicts the factor of safety for conditions where the primary strength of the geogrid is not parallel to the direction of movement or resultant 3D force.
- Finite-difference deformation analyses confirmed that a reduction in strength occurred along the soil–rock interface during the 8-year service life of the RSS due to deformations induced by the applied shear stresses and available groundwater. The deformation analyses also identified that the failure surface propagated from below the reinforced zone near the slope toe, behind the geogrids in the lower portion of the slope, and through the geogrids in the upper portion of the slope.
- Tension cracks observed approximately 2 years before the failure also appeared in the stress-deformation analyses when the tensile geogrid strains reached about 2%. This analysis suggests that stress-deformation analyses can be used to predict the applied shear stresses and strains and possible development of a failure surface through an RSS for future projects.
- As the shear strength of the soil–rock interface decreased from the peak strength toward the FSS, the lower portion of the slope underwent shear deformations, which transferred the shear stresses to the geogrid reinforcement, which resulted in its deformation and creep strength reduction, resulting in the failure of this RSS.

## Data Availability Statement

Some or all data, models, or code generated or used during the study are available from the first author by request.

## Acknowledgments

The contents and views in this paper are those of the individual authors and do not necessarily reflect those of any of the represented corporations, contractors, agencies, consultants, organizations, and/or contributors including Yeager Airport. The authors would like to thank RocScience Inc. for providing access to the

SLIDE3 software for this study and their technical support. The authors also acknowledge the assistance of Enok Cheon, who performed the 3D stability analyses using SLIDE3 while a graduate research assistant at the University of Illinois at Urbana-Champaign. The third author also appreciates the financial support of the National Science Foundation (NSF Award CMMI-1562010). The contents and views in this paper are those of the individual authors and do not necessarily reflect those of the National Science Foundation.

## References

- Akhtar, K., and T. D. Stark. 2017. "Importance of side resistance in a 3D stability analysis." In *Geotechnical Frontiers 2017: Walls and Slopes*, Geotechnical Special Publication 278, edited by T. L. Brandon and R. J. Valentine, 285–293. Reston, VA: ASCE.
- Arellano, W. D., and T. D. Stark. 2000. "Importance of three-dimensional slope stability analyses in practice." In *Slope Stability 2000: Proc., Sessions of Geo-Denver*, Geotechnical Special Publication 101, edited by D. V. Griffiths, G. A. Fenton, and T. R. Martin, 18–32. Reston, VA: ASCE.
- Berg, R. R., V. E. Chouery-Curtis, and C. H. Watson. 1989. "Critical failure planes in analysis of reinforced slopes." In *Proc., Geosynthetics '89 Conf.*, 269–278. San Diego: Industrial Fabrics Association International.
- Berg, R. R., J. G. Collin, T. P. Taylor, and C. F. Watts. 2020. "Case history on failure of a 67 M tall reinforced soil slope." *Geotext. Geomembr.* 48 (6): 802–811. <https://doi.org/10.1016/j.geotextmem.2020.06.003>.
- Cheng, Y. M., and C. J. Yip. 2007. "Three-dimensional asymmetrical slope stability analysis extension of Bishop's, Janbu's, and Morgenstern-Price's techniques." *J. Geotech. Geoenviron. Eng.* 133 (12): 1544–1555. [https://doi.org/10.1061/\(ASCE\)1090-0241\(2007\)133:12\(1544\)](https://doi.org/10.1061/(ASCE)1090-0241(2007)133:12(1544)).
- Huang, C., C. Tsai, and Y. Chen. 2002. "Generalized method for three-dimensional slope stability analysis." *J. Geotech. Geoenviron. Eng.* 128 (10): 836–848. [https://doi.org/10.1061/\(ASCE\)1090-0241\(2002\)128:10\(836\)](https://doi.org/10.1061/(ASCE)1090-0241(2002)128:10(836)).
- Itasca Consulting Group. 2018. "FLAC: Fast Lagrangian analysis of continuum software and user's guide." Accessed April 22, 2018. <https://www.itascacg.com/software/FLAC>.
- Janbu, N. 1954. *Stability analysis of slopes with dimensionless parameters*. Soil Mechanics Series, No. 46. Cambridge, MA: Harvard Univ.
- Lade, P. V. 2010. "The mechanics of surficial failure in soil slopes." *Eng. Geol.* 114 (1–2): 57–64. <https://doi.org/10.1016/j.enggeo.2010.04.003>.
- Lostumbo, J. 2010. "Yeager Airport runway extension: Tallest known 1H:1V slope in US." In *Proc., Geo-Institute Specialty Conf., Geo-Florida 2010: Advances in Analysis, Modeling & Design*, 2502–2510. Reston, VA: ASCE.
- Mesri, G., and M. Shahien. 2003. "Residual shear strength mobilized in first-time slope failures." *J. Geotech. Geoenviron. Eng.* 129 (1): 12–31. [https://doi.org/10.1061/\(ASCE\)1090-0241\(2003\)129:1\(12\)](https://doi.org/10.1061/(ASCE)1090-0241(2003)129:1(12)).
- Rocscience. 2017. *SLIDE3: Three-dimensional slope stability software and user's guide*. Toronto: Rocscience.
- Rocscience. 2018. *SLIDE: Two-dimensional slope stability software and user's guide*. Toronto: Rocscience.
- Seed, R., J. Mitchell, and M. Chang. 1993. "The Kettleman Hills landfill failure: A retrospective view of the failure investigations and lessons learned." Accessed January 20, 2018. <https://scholarsmine.mst.edu/cgi/viewcontent.cgi?article=2264&context=icchge>.
- Seed, R. B., J. K. Mitchell, and H. B. Seed. 1990. "Kettleman Hills waste landfill slope failure. II: Stability analysis." *J. Geotech. Eng.* 116 (4): 669–690. [https://doi.org/10.1061/\(ASCE\)0733-9410\(1990\)116:4\(669\)](https://doi.org/10.1061/(ASCE)0733-9410(1990)116:4(669)).
- Spencer, E. 1967. "A method of analysis of the stability of embankments assuming parallel inter-slice forces." *Géotechnique* 17 (1): 11–26. <https://doi.org/10.1680/geot.1967.17.1.11>.
- Stark, T. D., and H. T. Eid. 1997. "Slope stability analyses in stiff fissured clays." *J. Geotech. Geoenviron. Eng.* 123 (4): 335–343. [https://doi.org/10.1061/\(ASCE\)1090-0241\(1997\)123:4\(335\)](https://doi.org/10.1061/(ASCE)1090-0241(1997)123:4(335)).
- Stark, T. D., and H. T. Eid. 1998. "Performance of three-dimensional slope stability methods in practice." *J. Geotech. Geoenviron. Eng.* 124 (11): 1049–1060. [https://doi.org/10.1061/\(ASCE\)1090-0241\(1998\)124:11\(1049\)](https://doi.org/10.1061/(ASCE)1090-0241(1998)124:11(1049)).
- Stark, T. D., and D. G. Ruffing. 2018. "Selecting minimum factors of safety for 3D slope stability analyses." In *Geo-Risk 2017: Reliability-Based Design and Code Developments*, Geotechnical Special Publication 283, edited by J. Huang, G. A. Fenton, L. Zhang, and D. V. Griffiths, 259–266. Reston, VA: ASCE.